

RESEARCH ARTICLE | JUNE 20 2023

Finite element analysis of transverse size effect on the pyroelectric $\text{Pb}(\text{In}_{1/2}\text{Nb}_{1/2})\text{O}_3\text{--Pb}(\text{Mg}_{1/3}\text{Nb}_{2/3})\text{O}_3\text{--PbTiO}_3$ thin film for infrared array applications

Special Collection: [Energy Conversion and Storage in Functional Dielectrics](#)


Liang Cao ; Jiasheng Wang; Qiaozhen Zhang  ; Zihua Duan ; Tao Wang ; Yanxue Tang ; Xiangyong Zhao ; Zibin Chen  ; Feifei Wang  




Appl. Phys. Lett. 122, 252901 (2023)

<https://doi.org/10.1063/5.0145118>







Nanotechnology &
Materials Science




Optics &
Photonics



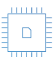
Impedance
Analysis




Scanning Probe
Microscopy



Sensors




Failure Analysis &
Semiconductors



Unlock the Full Spectrum.
From DC to 8.5 GHz.
Your Application. Measured.

[Find out more](#)



Finite element analysis of transverse size effect on the pyroelectric $\text{Pb}(\text{In}_{1/2}\text{Nb}_{1/2})\text{O}_3\text{-Pb}(\text{Mg}_{1/3}\text{Nb}_{2/3})\text{O}_3\text{-PbTiO}_3$ thin film for infrared array applications

Cite as: Appl. Phys. Lett. **122**, 252901 (2023); doi: [10.1063/5.0145118](https://doi.org/10.1063/5.0145118)

Submitted: 3 February 2023 · Accepted: 5 June 2023 ·

Published Online: 20 June 2023



View Online



Export Citation



CrossMark

Liang Cao,¹ Jiasheng Wang,¹ Qiaozhen Zhang,^{2,a)} Zhihua Duan,¹ Tao Wang,¹ Yanxue Tang,¹ Xiangyong Zhao,¹ Zibin Chen,^{3,a)} and Feifei Wang^{1,3,a)}

AFFILIATIONS

¹Key Laboratory of Optoelectronic Material and Device, Department of Physics, Shanghai Normal University, Shanghai 200234, China

²College of Information, Mechanical and Electrical Engineering, Shanghai Normal University, Shanghai 200234, China

³Department of Industrial and Systems Engineering, The Hong Kong Polytechnic University, Hong Kong, China

Note: This paper is part of the APL Special Collection on Energy Conversion and Storage in Functional Dielectrics.

a) Authors to whom correspondence should be addressed: zhangqz@shnu.edu.cn; zi-bin.chen@polyu.edu.hk;

and f_f_w@sohu.com

ABSTRACT

Exploring and revealing the influence of the pyroelectric thin film array element size on its structure and pyroelectric performance is crucial for designing integrated pyroelectric infrared detectors. In this work, the transverse size effect on the piezoelectric, dielectric, and especially the pyroelectric properties for a new-generation relaxor ferroelectric material $\text{Pb}(\text{In}_{1/2}\text{Nb}_{1/2})\text{O}_3\text{-Pb}(\text{Mg}_{1/3}\text{Nb}_{2/3})\text{O}_3\text{-PbTiO}_3$ (PIMNT) was studied by a finite element method. The lateral size-dependent piezoelectric and dielectric properties of the PIMNT thin film indicated that with the decrease in the transverse size, the piezoelectric constant d_{33} and relative dielectric constant ϵ_r increased substantially. The piezoelectric constant d_{33} and relative dielectric constant ϵ_r along (001) and (011) orientation increased faster than those along (111). A critical aspect ratio (in this paper, it was defined as radius/thickness) was found around 1:1 for three directions. We further discovered that the pyroelectric coefficient for PIMNT thin film along the (111) direction (the best crystallographic orientation for pyroelectric performance) decreased from 8.5×10^{-4} to 8.0×10^{-4} C/(m²·K) with the aspect ratio down to 0.01. The variation of the piezoelectric, dielectric, and pyroelectric properties originated from the declamping of the PIMNT thin film from the substrate. This finding gives insight into the transverse size effect on the electrical properties of new-generation relaxor PIMNT thin film and provides a guidance for designing high-performance infrared array detectors.

Published under an exclusive license by AIP Publishing. <https://doi.org/10.1063/5.0145118>

In recent years, pyroelectric uncooled infrared detectors have attracted much attention because of their distinguished advantages of small-size, wide spectrum response, and low power consumption. How to design and develop new materials or structures with high pyroelectric coefficient is critical to promote the device performance.^{1–4} The discovery of binary relaxor ferroelectric single crystal $\text{Pb}(\text{Mg}_{1/3}\text{Nb}_{2/3})\text{O}_3\text{-PbTiO}_3$ (PMNT) with high pyroelectric coefficient, high detection merit, and low thermal diffusion coefficient substantially improved the performance of infrared detectors.^{5–7} Correspondingly, the relaxor ferroelectric PMNT in the thin-film form attracted great attention, which was more favorable for integrated pyroelectric applications.^{8–10} However, the binary PMNT

with the composition around the morphotropic phase boundary has low ferroelectric rhombohedral to tetragonal phase transition temperature (only 70–80 °C), limiting its practical application.¹¹ Therefore, it is necessary to further increase the phase transition temperature to obtain better temperature stability.¹¹ Recently, the new-generation pyroelectric single crystals $\text{Pb}(\text{In}_{1/2}\text{Nb}_{1/2})\text{O}_3\text{-Pb}(\text{Mg}_{1/3}\text{Nb}_{2/3})\text{O}_3\text{-PbTiO}_3$ (PIMNT) and Mn-doped PIMNT were found to simultaneously possess high pyroelectric coefficient ($p \sim 10 \times 10^{-4}$ C/m²·K) and wider working temperature range (−100 °C to 110 °C) compared to binary PMNT single crystals.^{12,13} High-performance pyroelectric detectors based on PIMNT single crystals with enhanced signal stability were reported.¹⁴ Therefore,

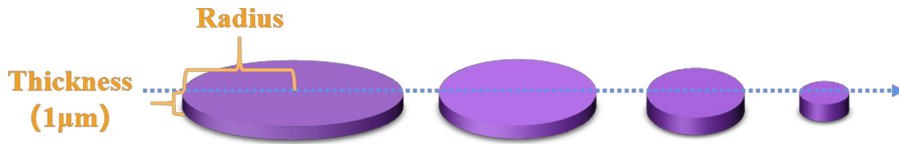


FIG. 1. Schematic diagram of cylindrical array element with aspect ratio decreasing.

the corresponding thin film counterparts attracted great attention. Ternary relaxor PIMNT thin films with high ferroelectric polarization and high pyroelectric coefficient have also recently been reported.^{15–17}

With the rapid development of infrared detection array technology, miniaturization, integration, and high pixel count have become the development trend of uncooled infrared detectors. The lateral size effect on the pyroelectric element for the array detector plays an important role. Previous studies on the lateral scaling effect in the binary PMNT film indicated that with the width-thickness ratio decreasing, there was an increase in the dielectric constant and ferroelectric polarization, reflecting the variation in the domain wall mobility and intrinsic response in laterally de-clamped PMNT.^{18–22} The effective piezoelectric constant increased from 40 to 50 to 160 pm/V at free sidewall under 200 kV/cm excitation.^{20,21} These limited studies were focused on binary PMNT and its piezoelectric and dielectric performance. Up to the present, the lateral scaling effect on new-generation PIMNT has not been reported. In addition to the piezoelectric and dielectric response, the pyroelectric response, which was influenced by the secondary piezoelectric effect, may also change with the lateral size decreasing. As a result, it is quite necessary to obtain the lateral scaling effect on the pyroelectric response in PIMNT, so as to guide its application in pyroelectric array detectors. Therefore, in this work, a three dimensional (3D) model was built, and the piezoelectric, dielectric, and pyroelectric properties were analyzed by the finite element method. The new-generation ternary relaxor ferroelectric PIMNT system was focused. The transverse size effect on the dielectric, piezoelectric, and especially the pyroelectric properties of PIMNT was investigated and the mechanism was discussed.

When studying the influence of different orientations on the electrical properties of PIMNT thin film array with a transverse size effect, the cylindrical shape was taken as an example in this work and the thickness was kept constant while the radius decreased, as shown in Fig. 1. Three-dimensional finite element modeling (FEM) was carried out by commercial software COMSOL, and multiple physical fields simulation was performed by the combination of the built-in piezoelectric effect coupling module, solid mechanics, and electrostatic boundary conditions.

Figure 2(a) shows the 3D FEM model used for piezoelectric and pyroelectric simulation, which was composed of the upper gold electrode layer and the lower piezoelectric layer. The film thickness was set to 1 μm. The bottom surface of the piezoelectric layer was fixed and restrained as the terminal with 1 V. The upper surface of the piezoelectric layer was grounded. According to the piezoelectricity, deformation will be induced when subjected to an external electric field and d_{33} was calculated from the inverse piezoelectric effect,²³

$$d_{ij} = \frac{\partial S_i}{\partial E_j}, \quad (1)$$

where d is the piezoelectric coefficient, S is the strain of the piezoelectric layer, and E is the applied electric field. The strain and electric field

in formula (1) can be derived from the induced displacement and the voltage applied.

Regarding the lateral size effect on the pyroelectric properties, the PIMNT is a ferroelectric and has both pyroelectric and piezoelectric response. It is known that the pyroelectric coefficient of the material under constant stress is mainly composed of the primary pyroelectric coefficient (under complete clamping condition) and the secondary pyroelectric effect caused by the piezoelectric effect,²⁴

$$p_i^X = p_i^X + e_{ij}^T \alpha_j^X = p_i^X + d_{ij}^T c_{jk}^T \alpha_k^X, \quad (2)$$

where p^X is the pyroelectric coefficient under the stress-free condition, p^X is the intrinsic pyroelectric coefficient under complete clamping condition, e is the piezoelectric pressure constant, d is the piezoelectric strain constant, c is the elastic stiffness constant, and α is the thermal expansion coefficient. In practical application, thin film materials are generally partially clamped. At the moment, the pyroelectric coefficient is composed of the superposition of the primary pyroelectric coefficient and the secondary pyroelectric effect (caused by deformation due to thermal expansion and polarization change through piezoelectric effect under partial clamping),

$$p_i^{X'} = p_i^X + e_{ij}'^T \alpha_j^X = p_i^X + d_{ij}'^T c_{jk}^T \alpha_k^X, \quad (3)$$

where $p^{X'}$ is the pyroelectric coefficient under partial clamping and the e' and d' are the clamped piezoelectric pressure constant and strain constant, respectively. Thus, the pyroelectric coefficient under partial clamping can be obtained through the combination of (2) and (3),

$$p_i^{X'} = p_i^X + d_{ij}'^T c_{jk}^T \alpha_k^X - d_{ij}^T c_{jk}^T \alpha_k^X. \quad (4)$$

The variation of the piezoelectric strain constant $d_{ij}'^T$ under different clamping conditions was used to calculate the secondary pyroelectric coefficient during decreasing of the aspect ratio (in this paper, it was defined as radius/thickness).

Figure 2(b) shows the dielectric model, which was composed of the outer air domain and the inner piezoelectric layer. Considering the capacitance effect by the air coupling and its edge field, the computation

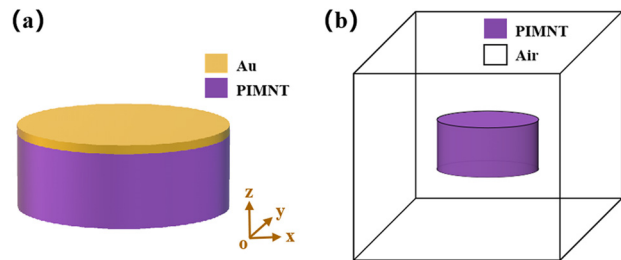


FIG. 2. Schematic diagram of 3D FEM model (a) for piezoelectric and pyroelectric simulation and (b) for dielectric property simulation.

TABLE I. Material constants of PIMNT single crystal utilized along the $\langle 001 \rangle$, $\langle 011 \rangle$, and $\langle 111 \rangle$ directions (Refs. 24–27).

Material constants	$\langle 001 \rangle^{25}$	$\langle 011 \rangle^{26}$	$\langle 111 \rangle^{24,27}$
$[C^E] \text{ (} 10^{10} \text{ N/m}^2 \text{)}$	$\begin{bmatrix} 12.2 & 11.3 & 10.8 & 0 & 0 & 0 \\ 11.3 & 12.2 & 10.8 & 0 & 0 & 0 \\ 10.8 & 10.8 & 11.2 & 0 & 0 & 0 \\ 0 & 0 & 0 & 6.9 & 0 & 0 \\ 0 & 0 & 0 & 0 & 6.9 & 0 \\ 0 & 0 & 0 & 0 & 0 & 6.2 \end{bmatrix}$	$\begin{bmatrix} 21.45 & 15.01 & 8.01 & 0 & 0 & 0 \\ 15.01 & 17.37 & 14.10 & 0 & 0 & 0 \\ 8.01 & 14.10 & 15.26 & 0 & 0 & 0 \\ 0 & 0 & 0 & 6.37 & 0 & 0 \\ 0 & 0 & 0 & 0 & 0.48 & 0 \\ 0 & 0 & 0 & 0 & 0 & 4.56 \end{bmatrix}$	$\begin{bmatrix} 20.96 & 6.46 & 8.29 & 2.66 & 0 & 0 \\ 8.29 & 20.96 & 6.46 & -2.66 & 0 & 0 \\ 6.46 & 6.46 & 17.65 & 0 & 0 & 0 \\ 2.66 & -2.66 & 0 & 2.10 & 0 & 0 \\ 0 & 0 & 0 & 0 & 2.10 & 2.66 \\ 0 & 0 & 0 & 0 & 2.66 & 6.33 \end{bmatrix}$
$[e] \text{ (C/m}^2 \text{)}$	$\begin{bmatrix} 0 & 0 & 0 & 0 & 16 & 0 \\ 0 & 0 & 0 & 16 & 0 & 0 \\ -2.7 & -2.7 & 18.6 & 0 & 0 & 0 \end{bmatrix}$	$\begin{bmatrix} 0 & 0 & 0 & 0 & 16.10 & 0 \\ 0 & 0 & 0 & 10.32 & 0 & 0 \\ 1.44 & -5.50 & 16.47 & 0 & 0 & 0 \end{bmatrix}$	$\begin{bmatrix} 0 & 0 & 0 & 0 & 18.78 & -6.48 \\ -6.48 & 6.48 & 0 & 18.78 & 0 & 0 \\ -5.19 & -5.19 & 8.72 & 0 & 0 & 0 \end{bmatrix}$
$[\varepsilon^S]$	$\begin{bmatrix} 4736 & 0 & 0 \\ 0 & 4736 & 0 \\ 0 & 0 & 659 \end{bmatrix}$	$\begin{bmatrix} 713 & 0 & 0 \\ 0 & 1294 & 0 \\ 0 & 0 & 597 \end{bmatrix}$	$\begin{bmatrix} 870 & 0 & 0 \\ 0 & 870 & 0 \\ 0 & 0 & 601 \end{bmatrix}$
$\rho \text{ (kg/m}^3 \text{)}$	8198	8185	8102
$[\alpha_1] \text{ (} 10^{-5} \text{ K)}$	\	\	1
$[\alpha_3] \text{ (} 10^{-5} \text{ K)}$	\	\	-2

domain used to simulate the edge field must be large enough (much larger than the size of the capacitor) to achieve accurate simulation. Therefore, the lower surface of the piezoelectric layer was set to be fixed and grounded. The outer surface of the air zone was set as 0 V suspension potential. By using the relationship between capacitance and dielectric constant, the capacitance values under different transverse size can be obtained by simulation, and the relative permittivity can be obtained,

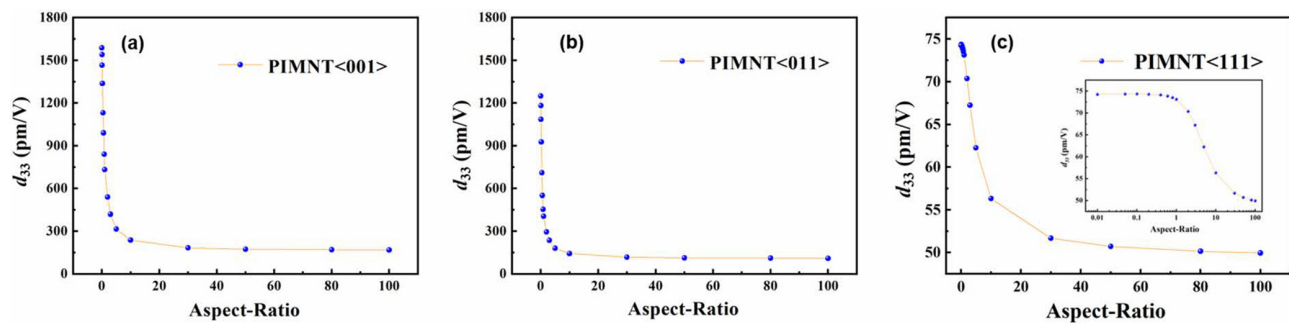
$$\varepsilon_r = \frac{C \times t}{\varepsilon_0 A}, \quad (5)$$

where C is the capacitance value of the element, ε_0 is the vacuum dielectric constant, ε_r is the relative permittivity, A is the electrode area, and t is the element thickness.

In the present work, the material parameters of the PIMNT ferroelectric single crystal were utilized. The unpoled PIMNT studied in this work was located in the rhombohedral phase region with $3m$

crystal symmetry at room temperature.^{24–27} After the crystal was poled along $\langle 001 \rangle$, $\langle 110 \rangle$, and $\langle 111 \rangle$ directions, macroscopic symmetries $4mm$, $mm2$, and $3m$ formed, respectively.^{24–27} The parameters used in our simulation were summarized in Table I.

By analysis of the 3D FEM model, the electric potential, stress, and displacement were obtained. The variation in the piezoelectric constant d_{33} was obtained from the surface displacement of the cross section for three different orientations of $\langle 001 \rangle$, $\langle 011 \rangle$, and $\langle 111 \rangle$. As shown in Fig. 3, when the transverse dimension of the element was $100 \mu\text{m}$, the piezoelectric constant d_{33} of $\langle 001 \rangle$ and $\langle 011 \rangle$ orientations was less than 300 pm/V and that of $\langle 111 \rangle$ orientation was less than 50 pm/V . With the decrease in aspect ratio from 100:1 to 10:1, the piezoelectric response of three directions first increased slowly from Fig. 3. When the aspect ratio further decreased, a sharp increase could be detected for the element along three directions. The piezoelectric constants of $\langle 001 \rangle$ and $\langle 011 \rangle$ -oriented PIMNT were higher than that of

**FIG. 3.** The influence of the aspect ratio on the piezoelectric constant of PIMNT with different orientations of (a) $\langle 001 \rangle$, (b) $\langle 011 \rangle$, and (c) $\langle 111 \rangle$.

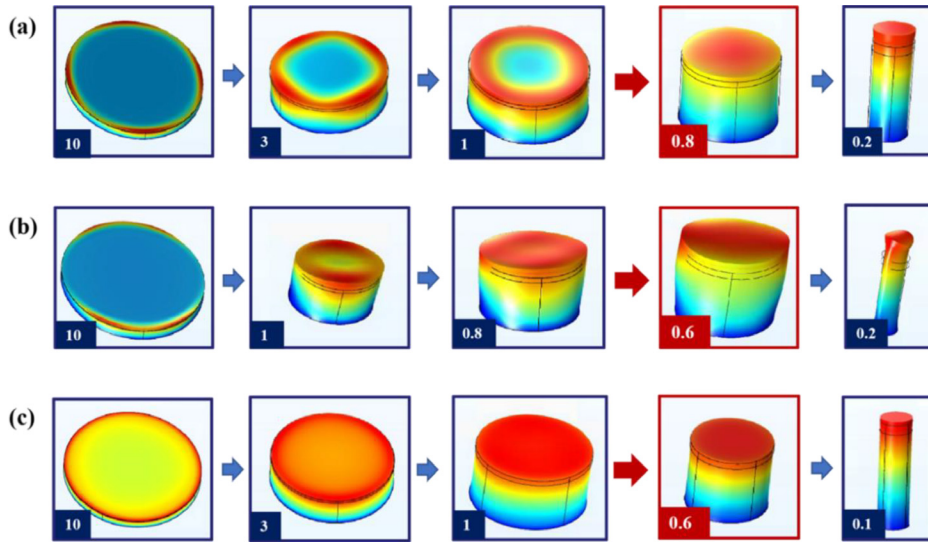


FIG. 4. 3D displacement shape of PIMNT array element with decreasing aspect ratio (shown in the left corner) along (a) $\langle 001 \rangle$, (b) $\langle 011 \rangle$, and (c) $\langle 111 \rangle$ directions.

$\langle 111 \rangle$ due to the formation of the engineered domain configurations. Under the aspect ratio of 0.01:1, the piezoelectric constant d_{33} along $\langle 001 \rangle$ direction reached 1539 pm/V, close to the d_{33} value of $\langle 001 \rangle$ -oriented free PIMNT single crystal.

Figure 4(a) shows the 3D displacement shape of the PIMNT array element with decreasing aspect ratio along the $\langle 001 \rangle$ oriented PIMNT film. When the aspect ratio of the array element was 10:1, the film exhibited the highest piezoelectric response near the edge along the orthogonal directions of the in-plane x axis and the y axis. When the aspect ratio of the array element reached 1:1, an outer ring-shaped protuberance was formed. With the aspect ratio further decreasing to 0.8:1, the inner concave “basin” phenomenon appeared. The near-edge position was no longer the peak response area of the displacement and the center position exhibited maximum displacement. Figure 4(b) shows the case for $\langle 011 \rangle$ orientation. The piezoelectric response increased obviously when the aspect ratio reached 1:1. Different from $\langle 001 \rangle$, the cylindrical film element with $\langle 011 \rangle$ orientation formed a half “rugby” shape displacement morphology. The critical point of displacement response along $\langle 011 \rangle$ orientation was

around 0.6:1. The two near-edge positions with the highest piezoelectric response turned to gather along the long axis of “rugby.” Figure 4(c) shows the results of PIMNT along $\langle 111 \rangle$ spontaneous polarization direction. Different from the $\langle 001 \rangle$ and $\langle 011 \rangle$ orientations, the overall piezoelectric response along $\langle 111 \rangle$ was relatively small. When the aspect ratio of the array element was 10:1, the near-edge area exhibited the maximum deformation. When the aspect ratio decreased to 1:1, the response of the surface tended to be more uniform. When the aspect ratio reached 0.6:1, the boundary response further weakened and the intermediate area also exhibited the maximum displacement.

Based on the analysis of the 3D displacement diagram, the displacement along the radius from the center of the element to the edge position was further calculated. Figure 5 shows the distribution of calculated piezoelectric constant d_{33} at each point along the radial direction. The d_{33} of the element with radius R ranging from 100 to $0.05 \mu\text{m}$ was illustrated. It can be found that the d_{33} variation trend is consistent with the 3D displacement diagram for the three representative crystallographic directions $\langle 001 \rangle$, $\langle 011 \rangle$, and $\langle 111 \rangle$. From Fig. 5(a), for $\langle 001 \rangle$

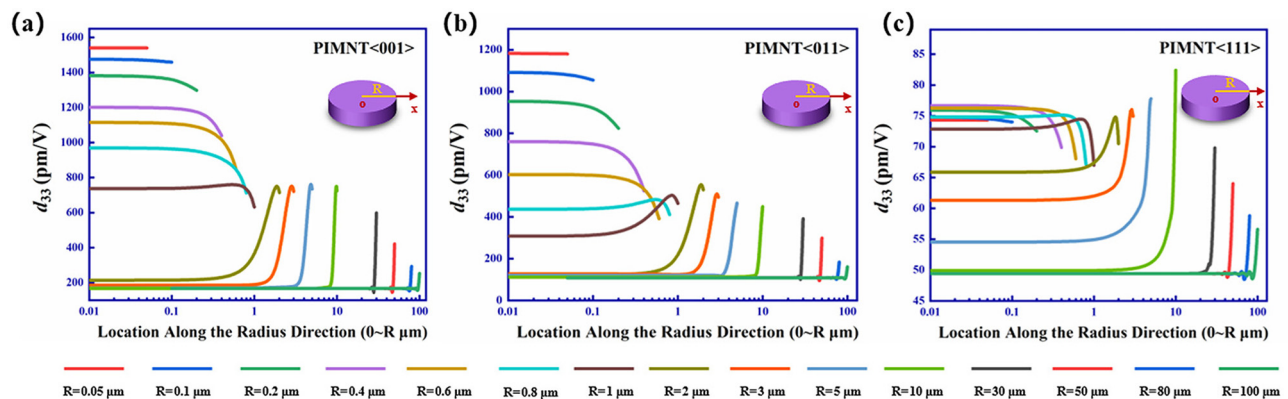


FIG. 5. Piezoelectric constant distribution of (a) $\langle 001 \rangle$, (b) $\langle 011 \rangle$, and (c) $\langle 111 \rangle$ oriented PIMNT along radius direction with decrease in the aspect ratio.

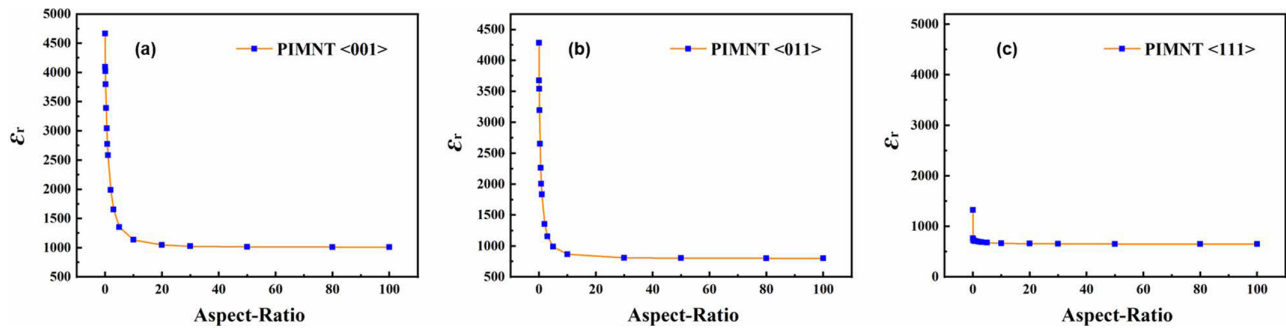


FIG. 6. The influence of the aspect ratio on the dielectric constant of (a) $\langle 001 \rangle$, (b) $\langle 011 \rangle$, and (c) $\langle 111 \rangle$ -oriented PIMNT.

orientation, when the radius was larger than $1 \mu\text{m}$, the variation trend of d_{33} at each point along the radial direction was similar to the result in binary PMNT.²⁰ The d_{33} with the strongest boundary effect is located near the edge of the element. The d_{33} variation along the $\langle 011 \rangle$ shown in Fig. 5(b) exhibited a similar trend to that of $\langle 001 \rangle$. In comparison, for $\langle 111 \rangle$ -oriented PIMNT thin film shown in Fig. 5(c), the piezoelectric response had another size inflection point around the aspect ratio of 0.4 where the piezoelectric response of the middle position decreased unexpectedly.

Figure 6 shows the influence of aspect ratio on dielectric properties of PIMNT thin film with different polarization directions. The dielectric constant for all three directions increased with the decrease in the aspect ratio. For the $\langle 111 \rangle$ -oriented PIMNT thin film shown in Fig. 6(c), the relative dielectric constant increased from 650 to 1323, with the aspect ratio decreasing from 100 to 0.01. The relative dielectric constant ϵ_r poled along $\langle 001 \rangle$ and $\langle 011 \rangle$ orientations (the engineered domain configuration was formed in the poled element) was obviously larger than that along $\langle 111 \rangle$ direction under the aspect ratio of 0.01. All these were related to the weakening of substrate clamping which improved the domain wall contribution and intrinsic lattice response.²⁰

The transverse size effect on the pyroelectric properties was obtained and shown in Fig. 7. During the simulation, the transverse size effect on the secondary pyroelectric effect was focused. The PIMNT thin film along $\langle 111 \rangle$ direction was analyzed, which exhibited the best pyroelectric response from previous work on PIMNT single crystal.²⁸ From Fig. 7, with the aspect ratio decreasing, the pyroelectric coefficient first decreased gently. When the aspect ratio further changed to around 10:1, a sharp decrease was observed. The pyroelectric coefficient decreased from 8.5×10^{-4} to $8.0 \times 10^{-4} \text{ C}/(\text{m}^2 \cdot \text{K})$ when the aspect ratio decreased to 0.01. This was due to the increase in the piezoelectric response during the lateral declamping process, which would increase the secondary pyroelectric coefficient.

From the above-mentioned result, it could be found that with the decrease in the transverse size, the substrate clamping stress and strain gradually released. This led to the reduced energy barriers for domain and domain wall motion, therefore, simultaneously enhancing the piezoelectric and dielectric properties exponentially below the critical aspect ratio. It was also found that the smaller the aspect ratio, the higher the piezoelectric and dielectric response, which were closer to those of the bulk single crystal. The local piezoelectric displacement along different poling directions exhibited similar symmetric distribution characteristics with their macroscopic crystal symmetry. The peak piezoelectric

response shifted from the edge to the center with the aspect ratio decreasing. The pyroelectric coefficient decreased slightly with the increase in the secondary piezoelectric effect contribution. These findings can provide an effective guide for understanding the lateral size effect on PIMNT and designing pyroelectric array detectors.

In summary, the transverse size effect on the piezoelectric, dielectric, and pyroelectric properties of new-generation PIMNT thin film with different polarization orientations were studied by FEM. It was found that with the decrease in the aspect ratio from 100 to 0.01, the d_{33} of the PIMNT element along $\langle 001 \rangle$ orientation increased from 178 to 1539 pm/V. The dielectric constant of the array element increased by nearly 2–5 times along three directions. The pyroelectric coefficient of the PIMNT element along $\langle 111 \rangle$ orientation decreased from 8.5×10^{-4} to $8.0 \times 10^{-4} \text{ C}/(\text{m}^2 \cdot \text{K})$. The mechanism responsible for the change in the piezoelectric, dielectric, and pyroelectric was the increased contribution from the domain wall motion and intrinsic lattice response. These findings can give insight into the transverse size effect on the PIMNT film and guide the design of high-performance integrated pyroelectric detectors.

This work was supported by the National Natural Science Foundation of China (Grant Nos. 11974250, 62175155, and

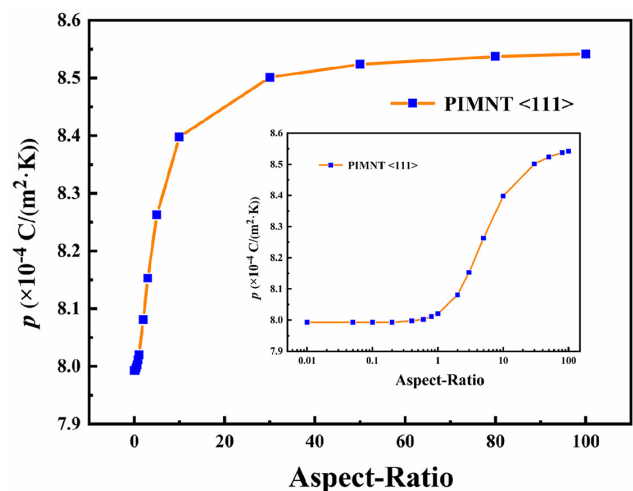


FIG. 7. Transverse size effect on the pyroelectric coefficient of $\langle 111 \rangle$ -oriented PIMNT thin film.

52172005), the National Natural Science Youth Foundation of China (Grant Nos. 11904233 and 12204393), the Research and Development Program in Significant Area of Guangzhou City (Grant No. 202206070001), and the Research Grant Council of Hong Kong Special Administrative Region, China (Project No. PolyU25300022). Z.B.C. would also like to express his sincere thanks for the financial support from the Research Office (Project Code: P0042733) of The Hong Kong Polytechnic University.

AUTHOR DECLARATIONS

Conflict of Interest

The authors have no conflicts to disclose.

Author Contributions

Liang Cao: Conceptualization (equal); Data curation (lead); Formal analysis (lead); Investigation (lead); Methodology (lead); Software (equal); Validation (equal); Writing – original draft (equal); Writing – review & editing (equal). **Jiasheng Wang:** Data curation (equal); Formal analysis (equal); Investigation (equal); Methodology (lead); Software (equal); Validation (equal); Writing – original draft (equal); Writing – review & editing (equal). **Qiaozhen Zhang:** Data curation (equal); Formal analysis (equal); Funding acquisition (equal); Investigation (equal); Software (equal); Supervision (equal); Writing – review & editing (equal). **Zhihua Duan:** Validation (equal); Writing – review & editing (equal). **Tao Wang:** Funding acquisition (equal); Validation (equal); Writing – review & editing (equal). **Yanxue Tang:** Validation (equal); Writing – review & editing (equal). **Xiangyong Zhao:** Funding acquisition (equal); Validation (equal); Writing – review & editing (equal). **Zibin Chen:** Conceptualization (equal); Funding acquisition (equal); Validation (equal); Writing – original draft (equal); Writing – review & editing (equal). **Feifei Wang:** Conceptualization (equal); Funding acquisition (equal); Supervision (equal); Validation (equal); Writing – original draft (equal); Writing – review & editing (equal).

DATA AVAILABILITY

The data that support the findings of this study are available from the corresponding authors upon reasonable request.

REFERENCES

- ¹J. Karthik, J. C. Agar, A. R. Damodaran, and L. W. Martin, *Phys. Rev. Lett.* **109**, 257602 (2012).
- ²F. Griggio, F. S. Jesse, A. Kumar, O. Ovchinnikov, H. Kim, T. N. Jackson, D. Damjanovic, S. V. Kalinin, and S. Troler-McKinstry, *Phys. Rev. Lett.* **108**, 157604 (2012).
- ³J. Karthik and L. W. Martin, *Phys. Rev. B* **84**, 024102 (2011).
- ⁴H. F. Zhao, W. Ren, and X. S. Liu, *Ceram. Int.* **43**, S464 (2017).
- ⁵Y. X. Tang and H. Luo, *Infrared Phys. Technol.* **52**, 180 (2009).
- ⁶N. Neumann, M. Es-Souni, and H. S. Luo, in *18th IEEE International Symposium on the Applications of Ferroelectrics (ISAF)* (IEEE, 2009), pp. 1–3.
- ⁷L. Li, X. Y. Zhao, X. B. Li, B. Ren, Q. Xu, Z. Liang, W. N. Di, L. R. Yang, H. S. Luo, X. M. Shao, J. X. Fang, N. Neumann, and J. Jiao, *Adv. Mater.* **26**, 2580 (2014).
- ⁸Y. X. Tang, B. Zhu, F. F. Wang, D. Z. Sun, Z. J. Hu, X. M. Qin, and W. Z. Shi, *Appl. Surf. Sci.* **371**, 160 (2016).
- ⁹Y. X. Tang, D. Zhou, Y. Tian, X. Li, F. F. Wang, D. Z. Sun, W. Z. Shi, L. Tian, J. L. Sun, X. J. Meng, and J. H. Chu, *J. Am. Ceram. Soc.* **95**, 1367 (2012).
- ¹⁰J. Tusnim, N. S. Jenifar, and M. Hasan, *Mater. Sci. Eng. C* **438**, 012029 (2018).
- ¹¹Q. Du, Y. Tang, X. Huang, F. Wang, X. Zhao, Z. Duan, X. Zhuang, W. Shi, J. Zhao, F. Liu, and H. Luo, *J. Am. Ceram. Soc.* **102**, 16600 (2019).
- ¹²L. Li, X. B. Li, X. Y. Zhao, B. Ren, Q. Xu, H. Q. Xu, H. S. Luo, X. Li, and X. M. Shao, *J. Alloys Compd.* **595**, 120 (2014).
- ¹³L. R. Yang, L. Li, X. Y. Zhao, Q. Xu, J. S. Ma, S. Wang, X. B. Li, W. N. Di, H. Q. Xu, and H. S. Luo, *J. Alloys Compd.* **695**, 760 (2017).
- ¹⁴Z. Li, F. Liu, Y. Tang, X. Zhao, T. Wang, Z. Duan, W. Shi, F. Wang, J. Jiao, and H. Luo, *J. Am. Ceram. Soc.* **104**, 17513 (2020).
- ¹⁵X. Huang, Y. Tang, F. Wang *et al.*, *J. Am. Ceram. Soc.* **105**, 18054 (2021).
- ¹⁶Z. Li, Y. Wang, Y. Tang, X. Zhao, T. Wang, Z. Duan, F. Wang, X. Li, C. Leung, and B. Fang, *J. Am. Ceram. Soc.* **104**, 17456 (2020).
- ¹⁷J. Wang, Z. Li, M. Zhang *et al.*, *J. Am. Ceram. Soc.* **105**, 18362 (2022).
- ¹⁸V. Nagarajan, A. Stanishevsky, L. Chen, T. Zhao, B. T. Liu, J. Melngailis, A. L. Roytburd, R. Ramesh *et al.*, *Appl. Phys. Lett.* **81**, 4215 (2002).
- ¹⁹R. Keech, S. Shetty, M. A. Kuroda, X. H. Liu, J. G. Martyna, D. M. Newns *et al.*, *J. Appl. Phys.* **115**, 234106 (2014).
- ²⁰R. Keech, L. H. Ye, J. L. Bosse, G. Esteves, J. Guerrier, J. L. Jones, M. A. Kuroda, B. D. Huey, and S. Troler-McKinstry, *Adv. Funct. Mater.* **27**, 1605014 (2017).
- ²¹C. Guo and H. Huang, *Microstructures* **2**, 2022021 (2022).
- ²²Z. B. Chen, F. Li, Q. W. Huang, F. Liu, F. F. Wang, S. P. Ringer, H. S. Luo, S. J. Zhang, L. Q. Chen, and X. Z. Liao, *Sci. Adv.* **6**, abc7156 (2020).
- ²³B. Jaffe, W. R. Cook, and H. Jaffe, *Piezoelectric Ceramics* (Academic Press, London, 1971).
- ²⁴Y. X. Tang, Ph.D. thesis (Shanghai Institute of Ceramics, Chinese Academy of Science, 2007).
- ²⁵X. Z. Liu, S. J. Zhang, J. Luo, T. R. Shrout, and W. W. Cao, *J. Appl. Phys.* **106**, 074112 (2009).
- ²⁶E. W. Sun, S. J. Zhang, J. Luo, T. R. Shrout, and W. W. Cao, *Appl. Phys. Lett.* **97**, 032902 (2010).
- ²⁷X. Z. Liu, S. J. Zhang, J. Luo, T. R. Shrout, and W. W. Cao, *Appl. Phys. Lett.* **96**, 012907 (2010).
- ²⁸Z. B. Jiang and Z. G. Ye, *Ferroelectrics* **557**, 9 (2020).